PNAS RESEARCH ARTICLE | BIOPHYSICS AND COMPUTATIONAL BIOLOGY

Cryo-EM structure of human voltage-gated sodium channel $Na_v1.6$

Xiao Fan[a,1,2], Jian Huang[a,1], Xueqin Jin[b], and Nieng Yan[a,b,2]

Contributed by Nieng Yan; received December 3, 2022; accepted December 27, 2022; reviewed by Ruobing Ren and Guanghui Yang

Voltage-gated sodium channel $Na_v1.6$ plays a crucial role in neuronal firing in the central nervous system (CNS). Aberrant function of $Na_v1.6$ may lead to epilepsy and other neurological disorders. Specific inhibitors of $Na_v1.6$ thus have therapeutic potentials. Here we present the cryo-EM structure of human $Na_v1.6$ in the presence of auxiliary subunits β1 and fibroblast growth factor homologous factor 2B (FHF2B) at an overall resolution of 3.1 Å. The overall structure represents an inactivated state with closed pore domain (PD) and all "up" voltage-sensing domains. A conserved carbohydrate–aromatic interaction involving Trp302 and Asn326, together with the β1 subunit, stabilizes the extracellular loop in repeat I. Apart from regular lipids that are resolved in the EM map, an unprecedented Y-shaped density that belongs to an unidentified molecule binds to the PD, revealing a potential site for developing $Na_v1.6$-specific blockers. Structural mapping of disease-related $Na_v1.6$ mutations provides insights into their pathogenic mechanism.

$Na_v1.6$ | ion channel | epilepsy | cryo-EM

Significance

Epilepsy is a chronic neurological disorder that affects approximately 50 million people of all ages worldwide. $Na_v1.6$, a voltage-gated sodium channel that mainly functions in the central nervous system, plays a key role in neuronal firing. Mutations in $Na_v1.6$ are associated with developmental and epileptic encephalopathy and other diseases. Here we report the cryo-EM structure of human $Na_v1.6$ co-expressed with β1 and FHF2B. An intact extracellular loop above the pore domain and a longer glycan chain in the first repeat are resolved, revealing a conserved interaction between Trp302 and the glycan on Asn326. An unprecedented density that belongs to a yet to be identified molecule provides clue to the development of antiepileptic drugs specifically targeting $Na_v1.6$.

Voltage-gated sodium (Na_v) channels govern the initiation and propagation of action potentials (1). Nine subtypes of human Na_v channels, $Na_v1.1$-$Na_v1.9$, share highly conserved sequences and execute this critical physiological function in different tissues. Among these, $Na_v1.6$, encoded by *SCN8A*, is dominantly expressed in the central nervous system (CNS) for neuronal firing (2–4). Abnormal activity of $Na_v1.6$ is associated with neurological disorders, exemplified by epilepsy (5, 6).

$Na_v1.6$ channels cluster at the axon initial segment (AIS), the site of action potential initiation (6–8). $Na_v1.6$ is the characteristic of higher persistent current and resurgent current, a unique electrophysiological property for repetitive firing in neurons (9–12). In the Purkinje cells from *Scn8a* knockout mice, the persistent current and resurgent current decreased by 70% and 90%, respectively, together with reduced repetitive firing (10). On the other hand, increased current by mutations can be epileptogenesis (13, 14). Specific inhibition of $Na_v1.6$ may thereby represent a potential strategy for developing antiepileptic seizure medications (ASMs)/antiepileptic drugs (AEDs) (15–17).

Na_v channels are subject to regulation by auxiliary subunits. Four different β subunits, β1 to β4, modulate the cellular trafficking and biophysical properties of Na_v channels (18–20). β1 is required for $Na_v1.6$-mediated repetitive firing at distal AIS (21). Fibroblast growth factor homologous factor 2 (FHF2), which represents another family of regulatory subunits, modifies the resurgent current through interacting with the carboxy-terminal domain (CTD) of $Na_v1.6$ (22, 23). Co-expression of the two auxiliary subunits increased the peak current in whole-cell recording (22).

Since the resolution revolution of cryogenic electron microscopy (cryo-EM), high-resolution structures of seven subtypes of human Na_v channels (24–31) have been resolved, leaving $Na_v1.6$ and $Na_v1.9$ the only outliers. Here we present the cryo-EM structure of full-length human $Na_v1.6$ co-expressed with β1 and FHF2B. Comparative structural analysis reveals conformational shift of the fourth voltage-sensing domain (VSD_{IV}) and a better resolved glycosylation site that stabilizes the extracellular loop in the first repeat (ECL_I). Disease-related mutations have been mapped to the structure for comprehensive analysis, which provides insights into potential antiepileptic treatment (32–35).

Results

Cryo-EM Analysis of Human Na_v 1.6 with β1 and FHF2B. Full-length human $Na_v1.6$ (α1 subunit) transiently expressed in HEK293T cells was characterized with whole-cell patch-clamping in the presence of β1 or β1 and FHF2B (Fig. 1*A*, and *SI Appendix*, Fig. S1 and Table S1) (23, 36). Co-expression of β1 alone or with FHF2B increased the conductance of $Na_v1.6$ (*SI Appendix*, Fig. S1*A*). The presence of both β1 and FHF2B led to right shifts of the activation and steady-state inactivation curves (Fig. 1*A*) as well as increased persistent current (*SI Appendix*, Fig. S1*B*).

Author contributions: X.F., J.H., and N.Y. designed research; X.F., J.H., and X.J. performed research; X.F., J.H., X.J., and N.Y. analyzed data; and X.F., J.H., and N.Y. wrote the paper.

Reviewers: R.R., Fudan University; and G.Y., China Agricultural University.

The authors declare no competing interest.

Copyright © 2023 the Author(s). Published by PNAS. This article is distributed under Creative Commons Attribution-NonCommercial-NoDerivatives License 4.0 (CC BY-NC-ND).

[1]X.F. and J.H. contributed equally to this work.

[2]To whom correspondence may be addressed. Email: xiaof@princeton.edu or nyan@princeton.edu.

This article contains supporting information online at https://www.pnas.org/lookup/suppl/doi:10.1073/pnas.2220578120/-/DCSupplemental.

Published January 25, 2023.

Downloaded from https://www.pnas.org by UNIVERSITY OF CAMBRIDGE on February 25, 2025 from IP address 131.111.5.201.

Consistent with the electrophysiological characterizations, co-expression with both β1 and FHF2B in HEK293F cells gave rise to a higher protein yield than $Na_v1.6$ alone or in the presence of β1 only. The channel complex was purified through a two-step affinity purification and size-exclusion chromatography (SEC) following our established protocol with minor modifications (*SI Appendix*, Fig. S2 *A* and *B*) (37). Freshly purified protein samples were used for cryo-EM grids preparation and data acquisition. Data processing in cryoSPARC yielded a 3D cryo-EM reconstruction at an overall resolution of 3.1 Å (Fig. 1*B* and *SI Appendix*, Figs. S2 *C* and *D* and S3).

The cryo-EM map immediately reveals a typical α1-β1 complex assembly (Fig. 1*C*) as seen in previously reported Na_v structures (27, 38). However, no reliable density was found to place FHF2B. In low-pass filtered EM maps of the $Na_v1.6$ complex, a blob of density that is considerably larger than that for the CTD in other Na_v maps is seen beneath the intracellular gate (*SI Appendix*, Fig. S4*F*). It may belong to FGF2B that attaches to the CTD, as their interaction has been confirmed in the crystal structure of $Na_v1.5$-CTD and FGF13 complex (39, 40). It is not unusual that cytosolic domains are poorly resolved or invisible in cryo-EM maps, likely due to their intrinsic flexibility. We will therefore focus on the well-resolved region of the $Na_v1.6$-β1 complex for structural analysis. Apart from the protein moieties, the EM reconstruction also contains a number of associated lipids, a glyco-diosgenin (GDN) molecule at the intracellular gate, and a total of nine glycosylation sites on the extracellular loops.

ECL_I Is Stabilized by β1 and the Conserved Asn326 Glycosylation. Compared to the other Na_v channels of known structures, the ECL_I is particularly long and resolved in full length in $Na_v1.6$ (Fig. 2 and *SI Appendix*, Fig. S4). ECL_I is involved in the association with the β1 subunit through an extensive hydrogen bond (H-bond) network (Fig. 2*B*). It is noted that ECLs, especially ECL_I, share lower sequence similarity than the transmembrane region among Na_v channels (Fig. 2 *A* and *D*). Nevertheless, even the most versatile regions still share a similar scaffold around the base body of the ECL_I (*SI Appendix*, Fig. S4 *A*, *B* and *D*).

For structural comparison, we used the ECL_I region (M274-S352) in $Na_v1.6$ as a reference for superimposition with the corresponding segments in other human Na_v structures through Matchmaker (*SI Appendix*, Fig. S4*A*) (41). The pairwise rmsd values between $Na_v1.6$ and $Na_v1.1$/$Na_v1.2$/$Na_v1.3$/$Na_v1.4$ for the ECL_I region range from 2.0 to 2.7 Å, indicating similar architecture among these subtypes (*SI Appendix*, Fig. S4*B*). In contrast, the rmsd values between $Na_v1.6$ and $Na_v1.5$/$Na_v1.7$/$Na_v1.8$ for ECL_I are much larger, ranging between 5.2 and 5.8 Å. The largest deviation occurs between $Na_v1.6$ and NaX, with the rmsd of 7.6 Å over 66 Cα atoms. Yet, NaX still employs the same interface for binding to β3, which is structurally similar to β1 (42).

A large oligosaccharide density was observed in the cryo-EM map of $Na_v1.6$, attaching to Asn326 (Fig. 2*C*). Clear branches were resolved in this glycan density, allowing us to trace nine monosaccharides unambiguously. According to the contour, we assigned the most compatible $GlcNAc_2Man_7$ glycan (Fig. 2*E*) from PDB 1GYA and refined it against the experimental density with restrains. By far, it is the largest density for a branched oligosaccharide modification in Na_v channels that have been structurally resolved.

The high quality of glycan density reveals two critical CH-π interactions between glycan and aromatic residues (Phe288 and Trp302) (Fig. 2*C*). These carbohydrate–aromatic interactions lock the glycan to the interface, resulting in a rigidified protein-glycan complex that could be well resolved via averaging in single particle analysis. ECL_I, which is sandwiched between the two interfaces,

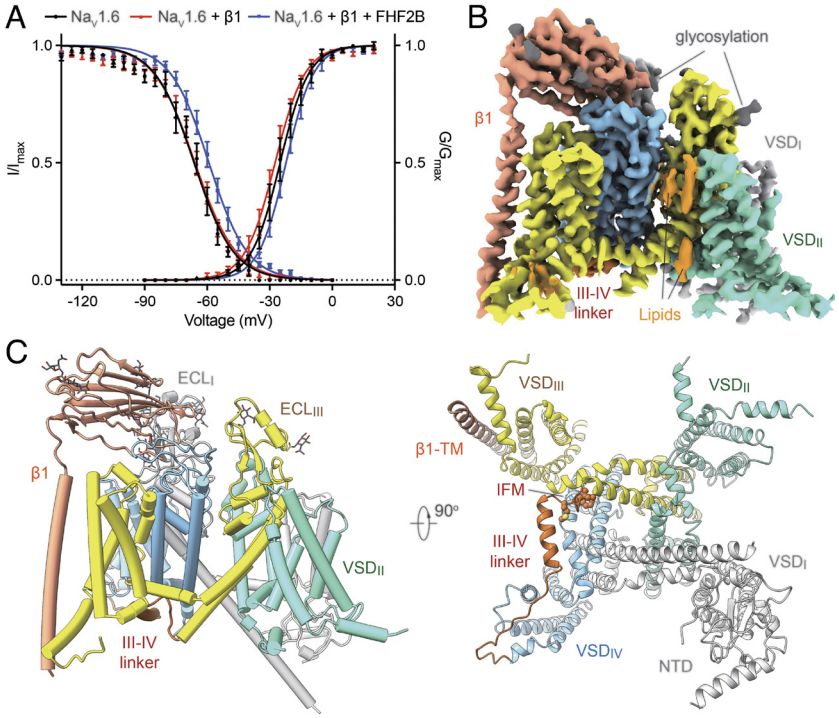

Fig. 1. Cryo-EM structure of human $Na_v1.6$-β1. (*A*) Electrophysiological properties of $Na_v1.6$ alone or co-expressed with the auxiliary subunits β1 and FHF2B in HEK293T cells. Shown here are the voltage-dependent activation and inactivation curves. Please refer to *Methods* and *SI Appendix*, Table S1 for details. (*B*) Cryo-EM map of the $Na_v1.6$ complex comprising the α1 (domain colored) and β1 (light salmon) subunits. The cytosolic III-IV linker is colored chocolate. Sugar moieties and lipids are colored gray and orange, respectively. The same color scheme is applied throughout the manuscript. (*C*) Overall structure of the $Na_v1.6$ complex in a *Side* view (*Left*) and a cytoplasmic view (*Right*). Sugar moieties are shown as sticks, and the IFM motif within the cytosolic III-IV linker is shown as spheres.

Downloaded from https://www.pnas.org by UNIVERSITY OF CAMBRIDGE on February 25, 2025 from IP address 131.111.5.201.

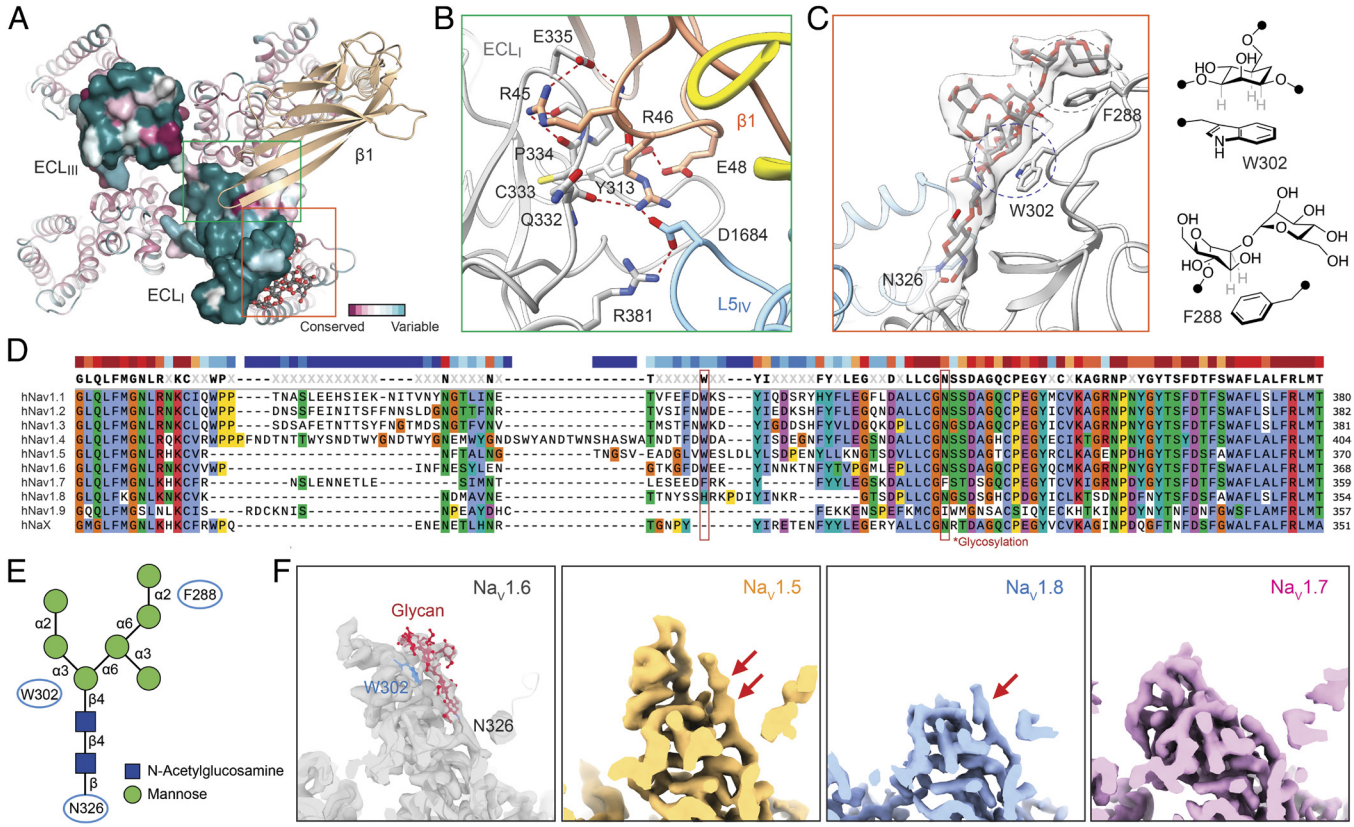

Fig. 2. ECL_I is sandwiched by β1 and the glycan attached to Asn326. (*A*) ECLs are the least conserved structural elements among Na_v subtypes. The conservation scores (calculated by ConSurf) of human Na_vs are color-coded and presented on the $Na_v1.6$ structure. The ECL_I and ECL_{III} region are shown as surface. Two interfaces, ECL_I-β1 and ECL_I-glycan, are highlighted in squares. (*B*) Extensive interactions between ECL_I and β1. Residues forming the hydrogen bond network, indicated by red, dashed lines, at the interface of ECL_I and β1 are shown. (*C*) Interactions between ECL_I and Asn326-glycan. Two aromatic residues, Trp302 and Phe288, are involved in the carbohydrate–aromatic interactions. The density in the *Left* panel is contoured at 5.2 σ. (*D*) Multiple sequence alignment of ECL_I in human Na_v subtypes. The alignment, calculated in Clustal X, is shaded in different colors based on sequence conservation and the chemical properties of the residues. The conserved glycosylation site (Asn326 in $Na_v1.6$) is indicated. (*E*) Schematic illustration of the chemical assembly of the branched N-$GlcNAc_2Man_7$ glycan. Related key residues are labeled in blue ovals. (*F*) Density variations of the corresponding glycan in different Na_v subtypes. Red arrows indicate the observed $GlcNAc_2$ and GlcNAc in $Na_v1.5$ (EMD-30850) and $Na_v1.8$ (EMD-32439), respectively.

ECL_I-glycan and ECL_I-β1, is thus stabilized and completely resolved in the EM map (Fig. 2*A*).

Multiple sequence alignment of the ECL_I regions shows that the Asn326 glycosylation site is highly conserved among Na_v channels, except $Na_v1.7$ and $Na_v1.9$. Trp302 is invariant in $Na_v1.1$-$Na_v1.6$. The corresponding loci $Na_v1.7$ and $Na_v1.8$ are occupied by Phe and His, respectively, but missing in $Na_v1.9$ (Fig. 2*D*). After examining all available structures and maps of Na_v channels, we identified Trp302 to be necessary for maintaining the carbohydrate–aromatic interaction at ECL_I-glycan interfaces.

Due to the intrinsic flexibility of oligosaccharides, glycans are usually resolved with a limited number of moieties that are in proximity to the modified residues. For the Na_v subtypes with both conserved Trp and Asn ($Na_v1.1$-$Na_v1.4$), similar glycan densities with the first branching mannose are discernible in the cryo-EM maps (*SI Appendix*, Fig. S4*C*). Unlike the subtypes above, the corresponding Trp301 in $Na_v1.5$ turns away from its position in $Na_v1.6$. Accordingly, only the first two GlcNAc moieties are visible (Fig. 2*F* and *SI Appendix*, Fig. S4*C*). $Na_v1.8$, which lacks the corresponding Trp, consistently displays an even shorter density for this glycosylation site (Fig. 2*F*) As expected, no glycosylation-related density is found in $Na_v1.7$, which lacks the corresponding Asn (Fig. 2 *D* and *F*).

Lipids in the Fenestrations of $Na_v1.6$. Densities that likely belong to endogenous lipids are observed surrounding the pore domain (PD) and penetrating fenestrations in the cryo-EM map of $Na_v1.6$ (Figs. 1*B* and 3 *A*). One density was assigned with a phosphatidylethanolamine (PE, 14:1/16:0) based on the shape of the head and the length of the tails (Fig. 3 *A* and *B*). The head group of PE projects into the central cavity and the two tails traverse through the II-III and III-IV fenestrations. Similar lipid densities have been observed in other human Na_v channels. However, an unprecedented density is seen at the IV-I fenestration site of $Na_v1.6$ (Fig. 3 *A* and *B*). This Y-shape density has a length of ~18 Å and a width of ~8 Å (*SI Appendix*, Fig. S4*E*). The long stem penetrates through the IV-I fenestration, and one of the branches points down to the intracellular gate.

Restricted by the amount of samples and technical limitations, we were not able to identify the chemical nature of this molecule. Nevertheless, the stable binding of a compound, which loosely clenches $S6_{IV}$, implicates a potential druggable site for $Na_v1.6$-specific inhibitors.

An Inactivated Conformation. As seen in other human Na_v structures, a GDN plugs into the intracellular gate, but the size of the gate is still not sufficient for permeating hydrated Na^+ ions (Fig. 3 *A* and *C*). All four VSDs are in the up conformation. Therefore, the overall structure of $Na_v1.6$ represents an inactivated state. During structural comparison, we noticed that VSD_{IV} exhibits more conformational variations than the other three VSDs among wild-type Na_v channels (Fig. 3*C*).

Downloaded from https://www.pnas.org by UNIVERSITY OF CAMBRIDGE on February 25, 2025 from IP address 131.111.5.201.

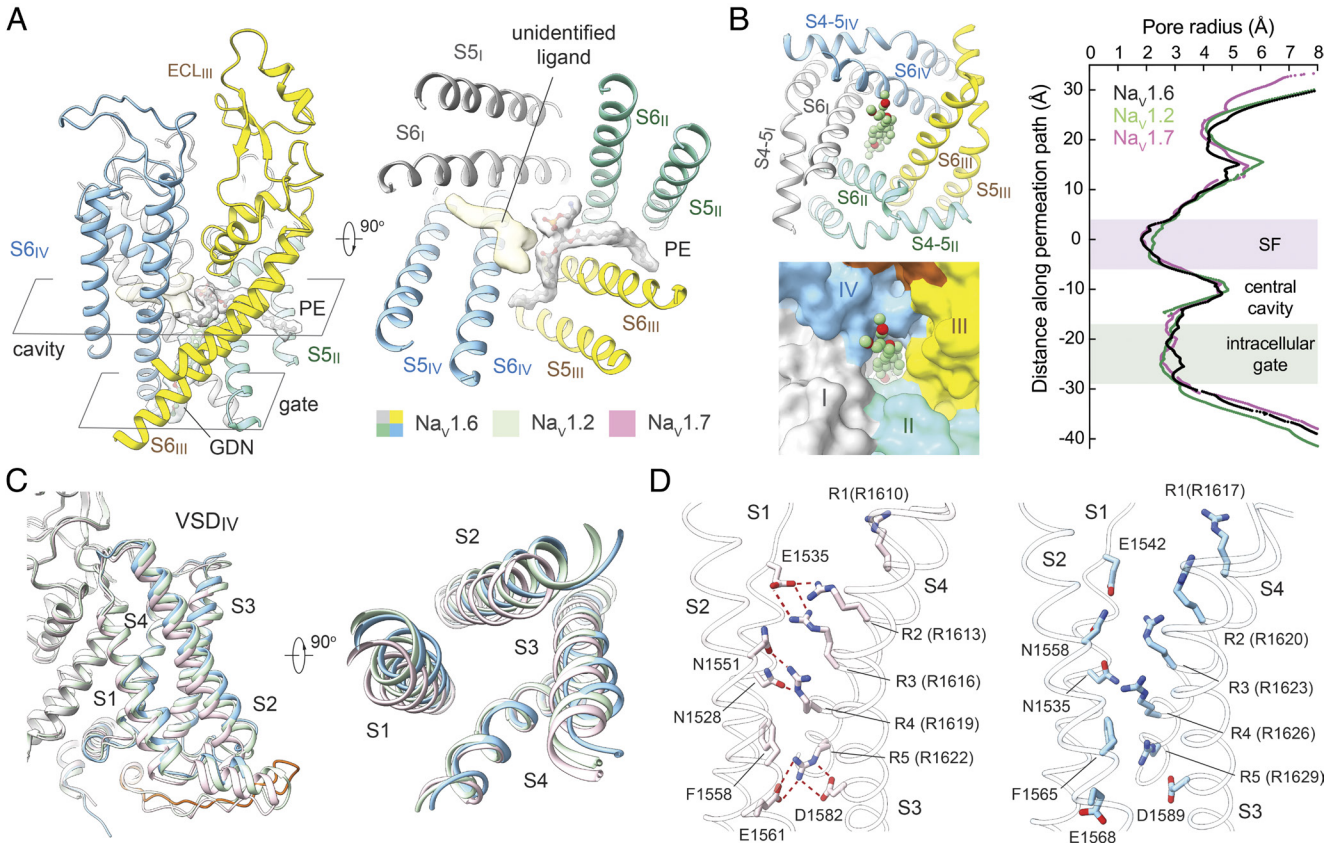

Fig. 3. Unique ligand density in the inactivated structure of $Na_v1.6$. (*A*) An unidentified density bound to the IV-I fenestration of the PD. A *Side* view and a *Top* view of the PD are shown. A putative PE is shown as gray ball-and-sticks in the semitransparent gray density. The density-colored pale yellow may belong to a molecule whose identity is unknown. (*B*) The intracellular gate of $Na_v1.6$ is penetrated by a GDN (green spheres). The permeation path of $Na_v1.6$ is calculated in HOLE, and the pore radii are superimposed with that of human $Na_v1.2$ (green) and $Na_v1.7$ (pink) (43). (*C*) VSD_{IV} exhibits a slightly different conformation in different Na_v channels. Structures of VSD_{IV} from $Na_v1.6$ (cyan), $Na_v1.2$ (green), and $Na_v1.7$ (pink) are superimposed relative to the overall structure. The PDB codes for $Na_v1.2$ and $Na_v1.7$ are 6J8E and 7W9K, respectively. Two perpendicular views are shown. (*D*) Distinct coordination of GC residues in VSD_{IV} of $Na_v1.7$ (*Left*) and $Na_v1.6$ (*Right*). The GC residues on $S4_{IV}$ and their coordinating residues on $S1_{IV}$-$S3_{IV}$ are shown as sticks, and the potential hydrogen bonds are shown as red-dashed lines.

As a tetrodotoxin (TTX)-sensitive channel, $Na_v1.6$ shares higher sequence identities with $Na_v1.1$ (77.6%), $Na_v1.2$ (77.2%), $Na_v1.3$ (76.1%), and $Na_v1.7$ (72.4%) than the three TTX-resistant subtypes. Despite overall structural similarities, $Na_v1.1$ and $Na_v1.2$ show similar but non-identical conformations of VSD_{IV} that slightly deviate from that in $Na_v1.3$ and $Na_v1.7$ (24–26, 37). $Na_v1.6$-VSD_{IV} is reminiscent of that in $Na_v1.2$ (PDB code:6J8E).

When $Na_v1.6$ and $Na_v1.7$ (PDB code: 7W9K) are superimposed relative to the α1 subunit, the $S4_{IV}$ helices align well, but $S1$–$S3_{IV}$ deviate disconcertedly (Fig. 3*C*). Consequently, coordination of the gating charge (GC) residues is different in these two structures despite a similar up conformation of $S4_{IV}$ (Fig. 3*D*). Compared to the extensive polar interactions between the GC residues and the adjacent polar residues on $S1$–$S3_{IV}$ in $Na_v1.7$ (Fig. 3*D*, *Left*), there is barely any polar coordination with the GC residues in $Na_v1.6$-VSD_{IV} (Fig. 3*D*, *Right*) owing to the motions of $S1$-$S3_{IV}$ relative to $S4_{IV}$ (Fig. 3*C*). The physiological relevance of these conformational deviations among different Na_v subtypes remains to be investigated.

Structural Mapping of Disease-Related Mutations in Human $Na_v1.6$. Human $Na_v1.6$ is associated with neurological disorders, such as developmental and epileptic encephalopathy 13 (DEE13), benign familial infantile seizures-5 (BFIS5), and familial myoclonus-2 (MYOCL2). The high-resolution structure of $Na_v1.6$ establishes the platform for mechanistic dissection of dozens of disease-related mutations.

We mapped a total of 48 loci reported as disease-related mutations in UniProt to the $Na_v1.6$ structure for analysis (Fig. 4 and *SI Appendix*, Table S2). Among these, 45/48 of the mutations are related to DEE13, with 18 mapped to the PD, 15 on VSDs, and seven on the CTD. In addition, two mutations are in the fast inactivation (FI) region and none on the selectivity filter (SF). As the CTD is poorly resolved, we will mainly focus on the PD and VSDs for discussion (Fig. 4*B*).

Among the disease-related residues, Leu407 and Phe1754 are the only two on the PD that point toward the central cavity. Phe260 and Val891, respectively, interact with VSD_{IV} and VSD_I through van der Waals contacts, suggesting their engagement in the electromechanical coupling. F260S and V891M may alter the local interactions, hence leading to changed coupling efficiencies between the PD and VSDs. The other disease-related residues on the PD mainly face adjacent S5 or S6 segments. Their mutations may either affect the stability of the PD or alter the conformations of the PD during the transitions between different channel states.

The distribution of disease-related loci on VSDs is highly asymmetric, with five each in VSD_I and VSD_{IV}, three in VSD_{II}, and only one in VSD_{III} (Fig. 4 and *SI Appendix*, Table S2). VSDs have been extensively characterized to detect membrane potential changes through the GC residues on the S4 helices. Mutation of GC residues can directly impact channel activation or/and inactivation through altered sensitivity to membrane potentials. Except for VSD_{III}, each VSD of $Na_v1.6$ harbors one DEE13-related mutation to GC

Downloaded from https://www.pnas.org by UNIVERSITY OF CAMBRIDGE on February 25, 2025 from IP address 131.111.5.201.

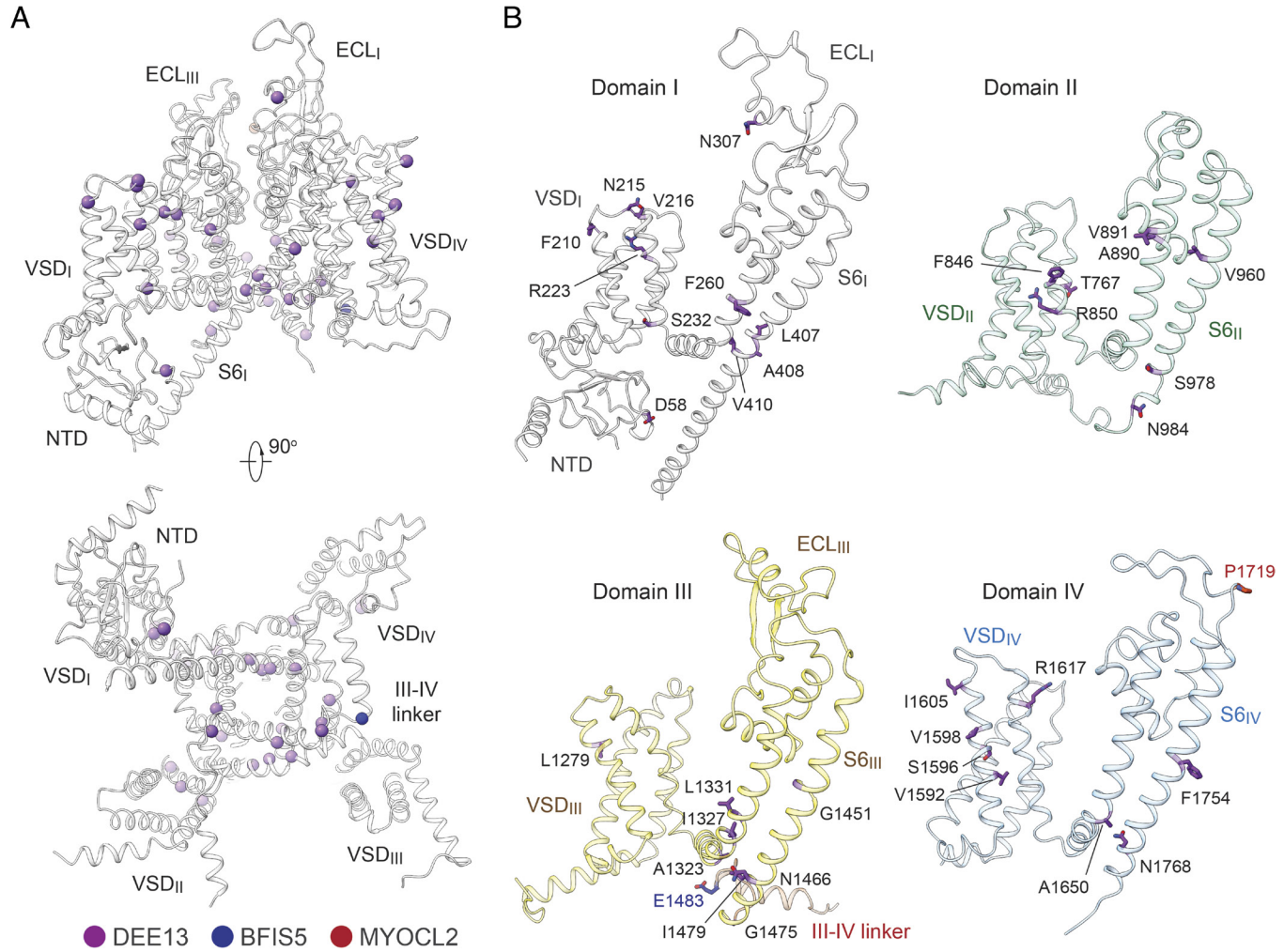

Fig. 4. Structural mapping of disease-related mutations in human $Na_v1.6$. (*A*) Mapping of the disease-associated mutations on the structure of $Na_v1.6$ in two perpendicular views. The Cα atoms of the disease-related residues are shown as spheres and colored for different types of disease. DEE13 (purple); BFIS5 (blue); MYOCL2 (red). (*B*) Mapping of the disease-related mutations in each domain of human $Na_v1.6$.

residues. These mutations (R223G, R850E, R850Q, and R1617Q) remove or reverse the positive charges. Many other mutations within VSDs may affect the intra-domain packing or interactions with lipids, which can affect structural stability or mobility during electromechanical coupling.

Discussion

$Na_v1.6$ is a drug target for the treatment of epileptic encephalopathy. Given the high degree of similarity in both sequence and architecture of all human Na_v subtypes, current Na_v-targeting ASMs/AEDs, such as carbamazepine, lacosamide, and phenytoin, are non-selective and at the risk of side effects. Therefore, subtype-specific ASMs/AEDs are preferred. Apart from the $Na_v1.6$-unique density observed in the PD (Fig. 3*A*), we have noticed the structural variations of VSD_{IV}, which has a wider pocket due to the displacement of $S1–S3_{IV}$ in $Na_v1.6$. VSD_{IV} domain represents a major target for most Na_v inhibitors of high affinity and selectivity (17, 26, 44). Structural variations of $Na_v1.6$-VSD_{IV} from other subtypes thus afford an important opportunity for drug development.

On the other hand, we have to acknowledge the current technical barriers for investigating structure-functional relationships. For example, among all available Na_v structures, no specific interactions between CTDs and any subunits have been observed in cryo-EM densities. A single mutation (R1872 > L/Q/W) on $Na_v1.6$-CTD could impair channel inactivation and increase channel activity (45, 46). In addition, co-expression of FHF2B, which selectively interacts with $Na_v1.6$-CTD, results in a depolarizing shift and increased persistent current of the channel. These cytosolic domains are usually poorly resolved or even invisible in cryo-EM maps, hindering a structural interpretation of their functional role.

Moreover, the unidentified ligand density at the IV-I fenestration represents another major technical barrier in the structure-based identification of endogenous ligands. Lipids, such as PIP2, have been identified from cryo-EM maps and shown to play an important structural and regulatory role (47). However, only in rare cases can these ligands be directly identified from high-resolution cryo-EM maps. Without reliable identification of the endogenous ligands, as in our present study, their functional role cannot be interpreted. Advanced and comprehensive analytical technologies, such as native mass spectrometry (48), are needed to address these important questions.

Notwithstanding the remaining questions, our structural analyses of human $Na_v1.6$ provide an important clue to its unique properties and establish the basis for the rational design of next-generation ASMs/AEDs.

Downloaded from https://www.pnas.org by UNIVERSITY OF CAMBRIDGE on February 25, 2025 from IP address 131.111.5.201.

Materials and Methods

Transient Expression of Human Na_v 1.6-β1-FHF2B in HEK293F Cells. Codon-optimized cDNA for full-length human $Na_v1.6$ (Uniprot Q9UQD0), a gift from Tsinghua University, was cloned into the pCAG vector with amino-terminal Twin-Strep-tag and FLAG-tag in tandem, while codon-optimized cDNAs for human Na_v β1 subunit (Uniprot Q07699) and human FHF2B (Uniprot Q92913-2) were cloned separately into the pCAG vector without any affinity tag. All the plasmids for transient expression were verified by PCR sequencing. Transient expression of $Na_v1.6$-β1-FHF2B adopted our established protocol with slight modifications (28). Briefly, HEK293F suspension cells (Thermo Fisher Scientific, R79007) were cultured at 37 °C in SMM 293T-II medium (Sino Biological Inc.). A plasmid mixture of 1.5 mg pCAG-$Na_v1.6$, 0.5 mg pCAG-β1 and 0.5 mg pCAG-FHF2B was pre-incubated with 4 mg 40-kDa linear polyethylenimines (Polysciences), then added into 1 L of cell culture with a cell density of 1.5 to 2.0 × 10^6 cells per mL for transient expression. Transfected cells were harvested approximately 48 h after transfection.

Protein Purification of Human Na_v1.6-β1-FHF2B Complexes. Following a similar protein purification protocol (49), 40 L cell pellets were resuspended in 25 mM Tris-HCl buffer (150 mM NaCl, pH 7.5) with protease inhibitor cocktail (Selleckchem). Additional 1% (w/v) n-dodecyl-β-D-maltopyranoside (DDM, Anatrace) and 0.1% (w/v) cholesteryl hemisuccinate Tris salt (CHS, Anatrace) were applied to the suspension for 2 h extraction at 4 °C. Supernatant was collected after centrifugation (16,000 g, 45 min) and incubated with anti-Flag M2 affinity gel (Sigma) for the first step affinity purification. The resin was rinsed with five column volume of buffer W (25 mM Tris-HCl pH 7.5, 150 mM NaCl, 0.06% GDN, and protease inhibitor cocktail) and eluted with buffer W supplemented with 0.2 mg mL^{-1} flag peptide (synthesized by GenScript). The eluent was then applied to pre-equilibrated Strep-Tactin Sepharose (IBA) resin for the second step affinity purification. After rinsing with buffer W, target proteins were eluted with buffer W supplemented with 2.5 mM desthiobiotin (IBA) followed by SEC (Superose 6 10/300 GL, GE Healthcare) in 25 mM Tris-HCl (pH 7.5), 150 mM NaCl, 0.02% GDN. The peak fractions were pooled and concentrated to a final concentration of about 7 mg mL^{-1}.

Whole-cell Electrophysiology. We applied the same protocol as in the previous publication with minor modifications (28, 31). HEK293T cells were transiently co-transfected with human Nav1.6 and eGFP with or without β1 and FHF2B in the presence of lipofectamine 2000 (Invitrogen). Then the whole-cell Na^+ currents were recorded with the same amplifier, software, and internal and bath solutions as before.

For voltage-dependent activation, cells were stepped from a holding potential of −120 mV (for 200 ms) to voltages ranging from −90 mV to +80 mV for 50 ms in 5 mV increments. For voltage dependence steady-state inactivation, cells were clamped at a holding potential of −90 mV and were applied to step pre-pulses from −130 mV to 0 mV for 50 ms with an increment of 5 mV. Then, the Na^+ currents were recorded at the test pulse of 0 mV for 50 ms. The activation and inactivation curves were analyzed as in previous studies. Persistent sodium current was measured as the mean inward current between 40 and 50 ms at the end of a 50-ms depolarization to 0 mV. Then the current was divided by the peak inward current at 0 mV to show persistent sodium current percentage.

Data were analyzed using Origin (OriginLab) and GraphPad Prism (GraphPad Software). All data points are presented as mean ± SEM, and n is the number of experimental cells. Statistical significance was assessed using one-way ANOVA analysis and extra sum-of-squares F test.

Cryo-EM Sample Preparation and Data Acquisition. Vitrobot MarK IV (Thermo Fisher) was set to 10 °C with 100% humidity. Filter papers (Ted Pella) were loaded before the cryosample preparation. Aliquots of 3 μL samples were loaded onto freshly glow-discharged gold Quantifoil grids (Au R1.2/1.3 300mesh, Quantifoil). A 4 s blotting was performed after the application of sample, followed with a rapid plunge-freezing into liquid ethane. Grids were stored in liquid nitrogen until loaded to a Titan Krios electron microscope (Thermo Fisher) for screen and data acquisition. This Krios was operated at 300 kV and equipped with a spherical aberration (Cs) image corrector. Super-resolution movie stacks were recorded by a Gatan Gif Quantum K2 summit direct electron detector (Gatan) in EFTEM mode with 20 eV slit at a nominal magnification of 105,000×, resulting in a calibrated pixel size of 0.557 Å. Based on calibrated dose rate, the exposure time for each stack was set to 5.6 s with a 0.175 s frame rate, yielding 32-frame stacks with a total electron dose of ~50 $e^-/Å^2$. SerialEM was used for target selection and automated data collection. During the data collection, each newly generated stack was monitored and pre-processed by Warp in real time to perform the drift correction, dose weighting, and CTF estimation. Summed and dose weighted micrographs were binned to a pixel size of 1.114 Å/pixel for the future data processing.

Cryo-EM Data Processing. 3,168 summed micrographs were imported into cryoSPRAC for patch CTF estimation (50). 45,472 particles in a small subset of 100 images were picked by blob picking to generate good 2D templates through 2D classification. After template picking and particle extraction, 3,097,800 particles were sent to three rounds of 2D classification. Only the best classes were selected in each round and provided 45,344 particles with clear secondary structural features in the third round 2D class averages. An initial 3D reference was generated from the selected 45,344 particles via Ab initio reconstruction and was applied to heterogenous refinement with three classes. The particles in each class after heterogenous refinement were classified by 2D classification, parallelly. Classes with membrane protein features were selected, and 771,584 particles were re-extracted in bin2. After five rounds of heterogenous refinement with two references, 146,393 particles in good class were extracted in bin1 for heterogenous refinement with higher-frequency information. 77,917 particles from the best 3D class were cleaned by another round of 2D classification to remove obvious junk classes. 74,103 particles were applied in non-uniform (NU) refinement to generate the final 3.1Å 3D reconstruction.

Model Building and Refinement. Model building for human $Na_v1.6$ used the initial model from $Na_v1.7$ (PDB: 7W9K), which comprises the same β1 auxiliary unit. The PDB model of 7W9K was docked manually and saved related to the $Na_v1.6$ EM density in Chimera (51). The refitted model was modified and adjusted in COOT based on sequence alignment in SnapGene and then refined against the corresponding map by the Real-space Refinement option in PHENIX with secondary structure and geometry restraints (52, 53). Validation for the model refinement is in *SI Appendix*, Table S3. The conservation score is calculated by ConSurf server (54).

Data, Materials, and Software Availability. All study data are included in the article and/or in *SI Appendix*. The cryo-EM map and atomic coordinates of human Nav1.6 complex have been deposited in the Electron Microscopy Data Bank (https://www.ebi.ac.uk/pdbe/emdb/) under accession number EMD-29082 and in the Protein Data Bank (https://www.rcsb.org) under accession number 8FHD, respectively.

ACKNOWLEDGMENTS. We thank the support by Paul Shao and Nan Yao for data collection at the cryo-EM facility at Princeton Imaging and Analysis Center, which is partially supported by the Princeton Center for Complex Materials, a NSF-MRSEC program (DMR-1420541). N.Y. was supported by the Shirley M. Tilghman endowed professorship from Princeton University in 2017–2022. X. F. has been supported by the HFSP long-term fellowship (LT000754) from the International Human Frontier Science Program Organization (HFSPO).

Author affiliations: [a]Department of Molecular Biology, Princeton University, Princeton, NJ 08544; and [b]State Key Laboratory of Membrane Biology, Beijing Frontier Research Center for Biological Structures, Tsinghua-Peking Joint Center for Life Sciences, School of Life Sciences, Tsinghua University, Beijing 100084, China

1. F. H. Yu, W. A. Catterall, Overview of the voltage-gated sodium channel family. *Genome Biol.* **4**, 207 (2003).
2. K. L. Schaller, D. M. Krzemien, P. J. Yarowsky, B. K. Krueger, J. H. Caldwell, A novel, abundant sodium channel expressed in neurons and glia. *J. Neurosci.* **15**, 3231–3242 (1995).
3. E. Tzoumaka *et al.*, Differential distribution of the tetrodotoxin-sensitive rPN4/NaCh6/Scn8a sodium channel in the nervous system. *J. Neurosci. Res.* **60**, 37–44 (2000).
4. W. Hu *et al.*, Distinct contributions of Na(v)1.6 and Na(v)1.2 in action potential initiation and backpropagation. *Nat. Neurosci.* **12**, 996–1002 (2009).
5. J. E. O'Brien, M. H. Meisler, Sodium channel SCN8A (Nav1.6): Properties and de novo mutations in epileptic encephalopathy and intellectual disability. *Front. Genet.* **4**, 213 (2013).
6. M. Royeck *et al.*, Role of axonal NaV1.6 sodium channels in action potential initiation of CA1 pyramidal neurons. *J. Neurophysiol.* **100**, 2361–2380 (2008).

Downloaded from https://www.pnas.org by UNIVERSITY OF CAMBRIDGE on February 25, 2025 from IP address 131.111.5.201.

7. A. Van Wart, G. Matthews, Impaired firing and cell-specific compensation in neurons lacking nav1.6 sodium channels. *J. Neurosci.* **26**, 7172–7180 (2006).
8. A. Lorincz, Z. Nusser, Cell-type-dependent molecular composition of the axon initial segment. *J. Neurosci.* **28**, 14329–14340 (2008).
9. A. H. Lewis, I. M. Raman, Resurgent current of voltage-gated Na(+) channels. *J. Physiol.* **592**, 4825–4838 (2014).
10. I. M. Raman, L. K. Sprunger, M. H. Meisler, B. P. Bean, Altered subthreshold sodium currents and disrupted firing patterns in Purkinje neurons of Scn8a mutant mice. *Neuron* **19**, 881–891 (1997).
11. Y. Chen *et al.*, Functional properties and differential neuromodulation of Na(v)1.6 channels. *Mol. Cell Neurosci.* **38**, 607–615 (2008).
12. C. E. Stafstrom, P. C. Schwindt, W. E. Crill, Repetitive firing in layer V neurons from cat neocortex in vitro. *J. Neurophysiol.* **52**, 264–277 (1984).
13. K. R. Veeramah *et al.*, De novo pathogenic SCN8A mutation identified by whole-genome sequencing of a family quartet affected by infantile epileptic encephalopathy and SUDEP. *Am. J. Hum. Genet.* **90**, 502–510 (2012).
14. L. Sole, J. L. Wagnon, M. M. Tamkun, Functional analysis of three Na(v)1.6 mutations causing early infantile epileptic encephalopathy. *Biochim. Biophys. Acta Mol. Basis Dis.* **1866**, 165959 (2020).
15. S. K. Bagal, B. E. Marron, R. M. Owen, R. I. Storer, N. A. Swain, Voltage gated sodium channels as drug discovery targets. *Channels* **9**, 360–366 (2015).
16. A. Fattorusso *et al.*, The pharmacoresistant epilepsy: An overview on existant and new emerging therapies. *Front. Neurol.* **12**, 674483 (2021).
17. M. Stevens, S. Peigneur, J. Tytgat, Neurotoxins and their binding areas on voltage-gated sodium channels. *Front. Pharmacol.* **2**, 71 (2011).
18. H. A. O'Malley, L. L. Isom, Sodium channel beta subunits: Emerging targets in channelopathies. *Annu. Rev. Physiol.* **77**, 481–504 (2015).
19. T. K. Aman *et al.*, Regulation of persistent Na current by interactions between beta subunits of voltage-gated Na channels. *J. Neurosci.* **29**, 2027–2042 (2009).
20. J. Zhao, M. E. O'Leary, M. Chahine, Regulation of Nav1.6 and Nav1.8 peripheral nerve Na+ channels by auxiliary beta-subunits. *J. Neurophysiol.* **106**, 608–619 (2011).
21. W. J. Brackenbury *et al.*, Functional reciprocity between Na+ channel Nav1.6 and beta1 subunits in the coordinated regulation of excitability and neurite outgrowth. *Proc. Natl. Acad. Sci. U.S.A.* **107**, 2283–2288 (2010).
22. A. M. Rush *et al.*, Differential modulation of sodium channel Na(v)1.6 by two members of the fibroblast growth factor homologous factor 2 subfamily. *Eur. J. Neurosci.* **23**, 2551–2562 (2006).
23. E. K. Wittmack *et al.*, Fibroblast growth factor homologous factor 2B: Association with Nav1.6 and selective colocalization at nodes of Ranvier of dorsal root axons. *J. Neurosci.* **24**, 6765–6775 (2004).
24. X. Pan *et al.*, Comparative structural analysis of human Na(v)1.1 and Na(v)1.5 reveals mutational hotspots for sodium channelopathies. *Proc. Natl. Acad. Sci. U.S.A.* **118**, e2100066118 (2021).
25. X. Pan *et al.*, Molecular basis for pore blockade of human Na(+) channel Na(v)1.2 by the mu-conotoxin KIIIA. *Science* **363**, 1309–1313 (2019).
26. X. Li *et al.*, Structural basis for modulation of human Na(V)1.3 by clinical drug and selective antagonist. *Nat. Commun.* **13**, 1286 (2022).
27. X. Pan *et al.*, Structure of the human voltage-gated sodium channel Na(v)1.4 in complex with beta1. *Science* **362**, 2486 (2018).
28. Z. Li *et al.*, Structure of human Na(v)1.5 reveals the fast inactivation-related segments as a mutational hotspot for the long QT syndrome. *Proc. Natl. Acad. Sci. U.S.A.* **118**, e2100069118 (2021).
29. D. Jiang *et al.*, Structure of the cardiac sodium channel. *Cell* **180**, 122–134.e110 (2020).
30. H. Shen, D. Liu, K. Wu, J. Lei, N. Yan, Structures of human Na(v)1.7 channel in complex with auxiliary subunits and animal toxins. *Science* **363**, 1303–1308 (2019).
31. X. Huang *et al.*, Structural basis for high-voltage activation and subtype-specific inhibition of human Na(v)1.8. *Proc. Natl. Acad. Sci. U.S.A.* **119**, e2208211119 (2022).
32. M. Rivara, M. K. Patel, L. Amori, V. Zuliani, Inhibition of NaV1.6 sodium channel currents by a novel series of 1,4-disubstituted-triazole derivatives obtained via copper-catalyzed click chemistry. *Bioorg. Med. Chem. Lett.* **22**, 6401–6404 (2012).
33. R. R. Patel, C. Barbosa, T. Brustovetsky, N. Brustovetsky, T. R. Cummins, Aberrant epilepsy-associated mutant Nav1.6 sodium channel activity can be targeted with cannabidiol. *Brain* **139**, 2164–2181 (2016).
34. T. Zaman, A. Abou Tayoun, E. M. Goldberg, A single-center SCN8A-related epilepsy cohort: Clinical, genetic, and physiologic characterization. *Ann. Clin. Transl. Neurol.* **6**, 1445–1455 (2019).
35. T. Focken *et al.*, Identification of CNS-penetrant aryl sulfonamides as isoform-selective Na(V)1.6 inhibitors with efficacy in mouse models of epilepsy. *J. Med. Chem.* **62**, 9618–9641 (2019).
36. C. Barbosa *et al.*, FHF2 isoforms differentially regulate Nav1.6-mediated resurgent sodium currents in dorsal root ganglion neurons. *Pflugers Arch.* **469**, 195–212 (2017).
37. G. Huang *et al.*, High-resolution structures of human Na(v)1.7 reveal gating modulation through alpha-pi helical transition of S6(IV). *Cell Rep.* **39**, 110735 (2022).
38. Z. Yan *et al.*, Structure of the Nav1.4-beta1 complex from electric eel. *Cell* **170**, 470–482.e411 (2017).
39. A. R. Gade, S. O. Marx, G. S. Pitt, An interaction between the III-IV linker and CTD in NaV1.5 confers regulation of inactivation by CaM and FHF. *J. Gen. Physiol.* **152**, e201912434 (2020).
40. C. Wang, B. C. Chung, H. Yan, S. Y. Lee, G. S. Pitt, Crystal structure of the ternary complex of a NaV C-terminal domain, a fibroblast growth factor homologous factor, and calmodulin. *Structure* **20**, 1167–1176 (2012).
41. E. C. Meng, E. F. Pettersen, G. S. Couch, C. C. Huang, T. E. Ferrin, Tools for integrated sequence-structure analysis with UCSF Chimera. *BMC Bioinform.* **7**, 339 (2006).
42. C. L. Noland *et al.*, Structure-guided unlocking of Na(X) reveals a non-selective tetrodotoxin-sensitive cation channel. *Nat. Commun.* **13**, 1416 (2022).
43. O. S. Smart, J. G. Neduvelil, X. Wang, B. A. Wallace, M. S. Sansom, HOLE: A program for the analysis of the pore dimensions of ion channel structural models. *J. Mol. Graph* **14**, 354–360, 376 (1996).
44. S. Ahuja *et al.*, Structural basis of Nav1.7 inhibition by an isoform-selective small-molecule antagonist. *Science* **350**, aac5464 (2015).
45. J. L. Wagnon *et al.*, Pathogenic mechanism of recurrent mutations of SCN8A in epileptic encephalopathy. *Ann. Clin. Transl. Neurol.* **3**, 114–123 (2016).
46. J. Larsen *et al.*, The phenotypic spectrum of SCN8A encephalopathy. *Neurology* **84**, 480–489 (2015).
47. S. Gao, X. Yao, N. Yan, Structure of human Ca(v)2.2 channel blocked by the painkiller ziconotide. *Nature* **596**, 143–147 (2021).
48. J. Gault *et al.*, Combining native and "omics" mass spectrometry to identify endogenous ligands bound to membrane proteins. *Nat. Methods* **17**, 505–508 (2020).
49. X. Yao *et al.*, Structures of the R-type human Ca(v)2.3 channel reveal conformational crosstalk of the intracellular segments. *Nat. Commun.* **13**, 7358 (2022).
50. A. Punjani, J. L. Rubinstein, D. J. Fleet, M. A. Brubaker, cryoSPARC: Algorithms for rapid unsupervised cryo-EM structure determination. *Nat. Methods* **14**, 290–296 (2017).
51. E. F. Pettersen *et al.*, UCSF Chimera–a visualization system for exploratory research and analysis. *J. Comput. Chem.* **25**, 1605–1612 (2004).
52. P. V. Afonine *et al.*, Towards automated crystallographic structure refinement with phenix.refine. *Acta Crystallogr. D Biol. Crystallogr.* **68**, 352–367 (2012).
53. P. Emsley, B. Lohkamp, W. G. Scott, K. Cowtan, Features and development of Coot. *Acta Crystallogr. D Biol. Crystallogr.* **66**, 486–501 (2010).
54. H. Ashkenazy *et al.*, ConSurf 2016: An improved methodology to estimate and visualize evolutionary conservation in macromolecules. *Nucleic Acids Res.* **44**, W344–W350 (2016).

Downloaded from https://www.pnas.org by UNIVERSITY OF CAMBRIDGE on February 25, 2025 from IP address 131.111.5.201.